ADVANCED SENSOR RESEARCH
Open Access
www.advsensorres.com

Responsive Mn-Ferrite Nanoparticles for Multicolor Magnetic Particle Imaging, Sensing, and Reactive Oxygen Species Degradation

*Fabian H. L. Starsich, Julia Feye, Robert Nißler, Gabriela Da Silva André, Elena Totter, Konrad Scheffler, Florian Thieben, Erik Mayr, Jochen Franke, Tobias Knopp, and Inge K. Herrmann**

New possibilities offered by Magnetic Particle Spectroscopy (MPS) and Imaging (MPI) are increasingly being recognized and may accelerate the introduction of MPI into clinical settings. As MPI is a tracer-based imaging method, the design and development of responsive tracers for functional imaging are particularly appealing. Here, Mn-ferrite ($Mn_xFe_{3-x}O_4$) nanoparticles with finely tuned magnetic properties and enzyme-like capabilities are reported as potential multifunctional theranostic agents. By adjusting the Mn content in the iron oxide matrix, the magnetic particle imaging signal of different tracers can be tweaked, allowing for the simultaneous quantitative detection of two different tracers in a multi-color approach. The Mn_2FeO_4 tracers exhibit potent enzyme-like catalytic properties, enabling degradation of reactive oxygen species, including H_2O_2 and OH^-. Due to the readily interchangeable oxidation states of Mn and Fe atoms in the crystal structure, a strong dependence of the magnetic properties is observed on H_2O_2 exposure, which can be exploited for sensing. This enables, for the first time, the sensing of reactive oxygen species based on magnetic particle spectroscopy and imaging, with sensitivity down to 25 µM H_2O_2 and complete sensor recovery over time. In summary, Mn-ferrite nanoparticles hold promising potential for imaging, sensing, and degradation of disease-relevant reactive oxygen species.

1. Introduction

Occlusion of the blood flow resulting in ischemia is the root cause of serious medical conditions, including undersupplied hearts (i.e., myocardial infarction) or brains (i.e., stroke) but also applies to livers, lungs (e.g., sleep apnea), and even multiple organs simultaneously.[1] The successful restoration of the blood flow represents a key step in the treatment of ischemia. However, upon reperfusion, the previously under-supplied body parts experience a sudden increase in oxygen concentration.[2] The reperfusion of hypoxic tissue with O_2 results in the production of a surplus of reactive oxygen species (ROS), which in turn causes cellular damage, a condition known as ischemic reperfusion injury. Under physiological normoxic conditions, ROS have important signaling functions and their concentration is regulated via superoxide dismutase (SOD) and catalase (CAT) enzymes, which degrade them into hydrogen peroxide and water, respectively. However, if the ROS concentration is elevated due to ischemic reperfusion, the enzymatic reaction rate is saturated, resulting in tissue injury.

Current clinical approaches to diagnosis and treatment monitoring of ischemia/reperfusion events are based on magnetic resonance imaging, computed tomography, or ultrasound imaging. However, these methods have limited sensitivity and spatiotem-

---

The ORCID identification number(s) for the author(s) of this article can be found under https://doi.org/10.1002/adsr.202400189

[+]Present address: Gericke AG, Althardstrasse 120, Regensdorf 8105, Switzerland

[++]Present address: Medical Microsystems Laboratory, Institute for Translational Medicine, Department of Health Sciences and Technology, ETH Zurich, Gloriastrasse 39, Zurich 8092, Switzerland

DOI: 10.1002/adsr.202400189

F. H. L. Starsich[+], J. Feye, R. Nißler, G. D. S. André, E. Totter[++], E. Mayr, I. K. Herrmann
Nanoparticle Systems Engineering Laboratory
Department of Mechanical and Process Engineering
ETH Zurich
Sonneggstrasse 3, Zurich 8092, Switzerland
E-mail: inge.herrmann@uzh.ch
F. H. L. Starsich[+], R. Nißler, G. D. S. André, E. Mayr, I. K. Herrmann
Laboratory for Particles-Biology Interactions
Department Materials Meet Life
Swiss Federal Laboratories for Materials Science and Technology (Empa)
Lerchenfeldstrasse 5, St. Gallen 9014, Switzerland

poral resolution, are based on ionizing radiation, and/or are expensive.[3] Magnetic particle imaging (MPI)[4] has been proposed as an emerging alternative to the latter methods for cardiovascular imaging[5] due to its high spatiotemporal resolution and background-free imaging capabilities.[6,7] The MPI technique is based on the detection of magnetic nanoparticles responding to an alternating magnetic field.[3] As it is a magnetic tracer-based method, it does not involve ionizing radiation exposure as does computed tomography (CT) and is not limited in penetration depth as opposed to optical imaging techniques. MPI has previously successfully been applied for the real-time imaging of stroke[6] or even a beating mouse heart,[8] illustrating the capabilities offered by the high spatiotemporal resolution. Interestingly, it can be expanded to allow multi-color imaging based on several distinct magnetic tracers, opening new possibilities for functional (molecular) imaging.[9]

As MPI is a tracer-based imaging method, the quality of an MPI scan directly depends on the characteristics of the used magnetic tracers.[3] To maximize resolution and sensitivity, an ideal MPI tracer should exhibit a steep magnetization curve (high susceptibility, rapid response), and a stable signal. So far, research has been focused on polymer-coated iron oxide particles such as Resovist as these are readily accessible and were FDA approved. Interestingly, the large material group of ferrites has not yet been investigated extensively as MPI tracers. The replacement of Fe atoms in the Fe_3O_4 crystal by bi- or trivalent atoms, such as Mn^{2+}, Zn^{2+}, or Gd^{3+} leads to the formation of interesting spinel structures with tunable magnetic properties. Silvestri et al. investigated various di- and tri-component nanocubes via magnetic particle spectroscopy and reported $Zn_{0.2}Fe_{2.8}O_4$ as a most promising candidate material.[10] Du et al. prepared $MnFe_2O_4$ nanoparticles for in vivo MPI and magnetic hyperthermia treatment.[11] Recently, we have reported flame-made non-stoichiometric Zn-ferrites as promising highly stable MPI tracers.[12] Flame synthesis allows for the production of ferrites with precisely tunable compositions,[13] sizes,[14] and morphologies on a large scale (up to kg h^{-1}).[15] On the one hand, this enables the straightforward investigation of particle structure-function correlations, and on the other hand, it offers a route to reproducible and scalable particle synthesis, which is instrumental for clinical translation once the particle tracers have been optimized.

Most interestingly, such ferrite-based catalytically active nanoparticles may also efficiently mimic antioxidant enzymes and act as so-called nanozymes.[16] Certain materials with two interchangeable oxidation states have been shown to catalyze the SOD and CAT reactions. Naturally occurring enzymes contain Fe, Mn, Zn, Cu, or Ni as active reaction sites. In addition to CeO_2[17,18] and noble metal nanoparticles,[19] iron[20] and manganese oxide[21] nanozymes have been reported and show excellent catalytic properties due to their spinel structure. Next to the therapeutic degradation of ROS by such nanozymes, also the localization and quantification of ROS are crucial to adequately manage or even prevent reperfusion damage. The accurate detection of radicals, however, is a challenging task due to their high reactivity and short half-life. Sensing via fluorescent dyes[22] or nanoparticles[23,24] and electrochemical methods[25] have been proposed and offer in vivo imaging capabilities. Nevertheless, a real-time non-invasive technique for the accurate detection of ROS is still heavily sought after.

Here, we present flame-synthesized ferrite MPI tracer candidate materials with tunable properties. We demonstrate that the tracers can be engineered to exhibit pronounced nanozyme activity, effectively protecting cells from oxidative stress. Additionally, the different tracers exhibit distinctly different magnetic behavior detectable in MPI, hence allowing multi-color imaging and distinction of different MPI tracers. Finally, we demonstrate that such ferrites may even be employed as sensor candidate materials as their magnetic properties change as a function of local ROS concentration.

2. Results and Discussion

2.1. Synthesis and Characterization of Mn-Ferrite Tracers

Magnetically and enzymatically active $Mn_xFe_{3-x}O_4$ nanoparticles of different stoichiometry (x = 0.2, 0.5, 1, 2, 3) were produced via scalable and dry flame spray pyrolysis. **Figure 1** depicts scanning transmission electron microscopy images of the $Mn_{0.2}Fe_{2.8}O_4$ (a) and Mn_2FeO_4 (b) structures. Both systems show a fractal-like morphology characteristic of flame-made nanoparticles. The primary particles show an average diameter d_{STEM} of 9.6 nm ($Mn_{0.2}Fe_{2.8}O_4$) and 10.6 nm (Mn_2FeO_4), and a respective geometric standard deviation σ_g of 1.4 and 1.3. These values are in good agreement with the obtained crystal sizes (see Table S1, Supporting Information), which indicates monocrystallinity. The primary particles are sintered together into larger aggregates fol-

---

J. Feye
Faculty of Engineering
Baden-Württemberg Cooperative State University Karlsruhe and
Institute of Inorganic Chemistry
Karlsruhe Institute of Technology
76131 Karlsruhe, Germany
R. Nißler, E. Mayr, I. K. Herrmann
Ingenuity Lab
Balgrist University Hospital
Forchstrasse 340, Zurich 8008, Switzerland
K. Scheffler, F. Thieben, T. Knopp
Section for Biomedical Imaging
University Medical Center Hamburg-Eppendorf
Lottestraße 55, 22529 Hamburg, Germany
K. Scheffler, F. Thieben, T. Knopp
Institute for Biomedical Imaging
Hamburg University of Technology
Am Schwarzenberg-Campus 3, 21073 Hamburg, Germany
E. Mayr
Laboratory for Magnetic and Functional Thin Films
Swiss Federal Laboratories for Materials Science and Technology (Empa)
Überlandstrasse 129, Dübendorf 8600, Switerland
J. Franke
Bruker
BioSpin GmbH Co. KG
Preclinical Imaging Division
76275 Ettlingen, Germany
I. K. Herrmann
Faculty of Medicine
University of Zurich
Rämistrasse 71, Zurich 8006, Switzerland
T. Knopp
Fraunhofer Research Institution for Individualized and Cell-based
Medical Engineering IMTE
Mönkhofer Weg 239a, 23562 Lübeck, Germany

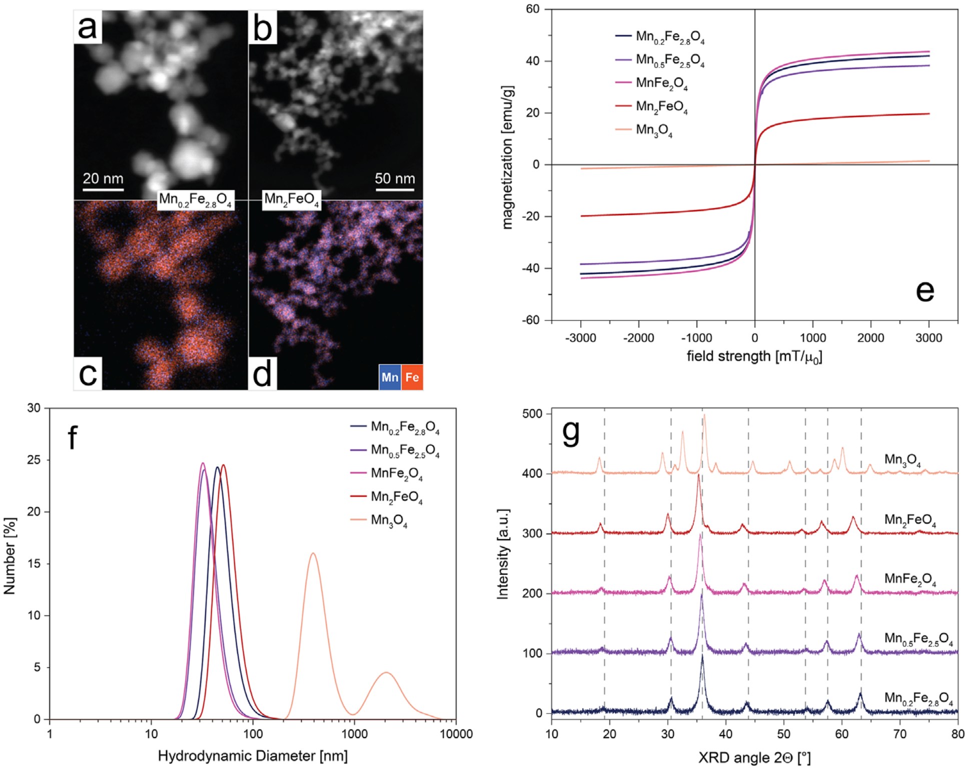

Figure 1. Scanning transmission electron microscopy images of a) $Mn_{0.2}Fe_{2.8}O_4$ and b) Mn_2FeO_4 nanoparticles with corresponding elemental mappings c,d) for Mn (blue) and Fe(red) below. e) Magnetization curves, f) number distribution of hydrodynamic diameters, and g) X-ray diffraction patterns of prepared particles. Dashed lines indicate XRD-peak positions of Fe_3O_4 spinel crystal phase.

lowing the high temperatures the materials experience during the synthesis. These aggregates form larger agglomerates held together via weak van der Waals forces. Hydrodynamic size measurements (Figure 1f) following strong sonication of these particles suggest an aggregate diameter of 30–50 nm, with very similar d_{DLS} for the different Fe-containing structures. Only pure Mn_3O_4 attained a d_{DLS} of ≈396 nm, which indicates substantial agglomeration. This can be explained by the reduced surface charge of Mn_3O_4 (1.8 mV) compared to $Mn_{0.2}Fe_{2.8}O_4$ (24.7 mV). Particle suspension in water formed a colloidal dispersion that remained stable for several days (Figure S1, Supporting Information). The composition of the material was analyzed by elemental mapping, which is depicted in Figure 1c,d for $Mn_{0.2}Fe_{2.8}O_4$ and Mn_2FeO_4, respectively. The images indicate a homogeneous incorporation of the Mn atoms into the iron oxide matrix, which is further verified by the X-ray diffraction patterns, presented in Figure 1g and Figure S2 (Supporting Information). These results are in excellent agreement with Mn_3O_4[26] and ferrite[13,14] structures previously prepared by flame spray pyrolysis, where the successful incorporation of Zn and/or Gd into the iron oxide crystal was shown. Already small amounts of Mn (or Zn/Gd) lead to the formation of the spinel crystal structure opposed to the maghemite phase (Fe_2O_3) typically obtained in the strongly oxidizing conditions of flame synthesis.[27] A pure spinel magnetite phase (Fe_3O_4) is not readily accessible via flame spray pyrolysis and was approximated via low-content Mn-ferrites in this work.

The incorporation of Mn atoms into the iron oxide nanoparticles enables the fine-tuning of their magnetic properties. Figure 1e shows the magnetization as a function of the applied field (i.e., hysteresis curves) for the various Mn-ferrites and pure Mn_3O_4. All ferrite particles attain S-shaped magnetization curves indicating ferro-/ferrimagnetic behavior. Furthermore, the coercivities H_c for all samples remained close to zero (below 2 mT/μ_0, see Table S1, Supporting Information), which suggests that the systems were measured in a superparamagnetic state. The saturation magnetizations M_s of the particles with low Mn content lie at ≈40 emu g^{-1}. $MnFe_2O_4$ shows the strongest magnetization, while Mn_2FeO_4 has a reduced saturation magnetization down to 20 emu g^{-1}. Pure Mn_3O_4 shows only very weak paramagnetic properties, as expected. M_s values for flame-made Fe_2O_3 nanoparticles with comparable sizes of 38.8 emu g^{-1} and H_c of 6 mT have been reported.[28] Values for $MnFe_2O_4$ vary in the range of 39 emu g^{-1}[29] to 74 emu g^{-1},[30] depending on particle size and synthesis method.

As evident from the magnetization curves shown above, the magnetic properties of the particles can be influenced by the Mn content in the iron oxide crystal. This is further investigated via magnetic particle spectroscopy (MPS) measurements, which also give first insights into the particles' performance as MPI tracers. **Figure 2a** depicts the MPS spectra amplitudes at selected harmonics measured at 6 and 20 mT applied field. As expected, the amplitudes drop faster below the detection limit (10^{-13} [a.u.] at a smaller applied field. At the 3rd harmonic, which is frequently investigated as the main MPS frequency, the particles with low Mn contents show a clearly stronger signal. At high harmonics such as the 45th and 75th, Mn_2FeO_4 reaches amplitudes similar to

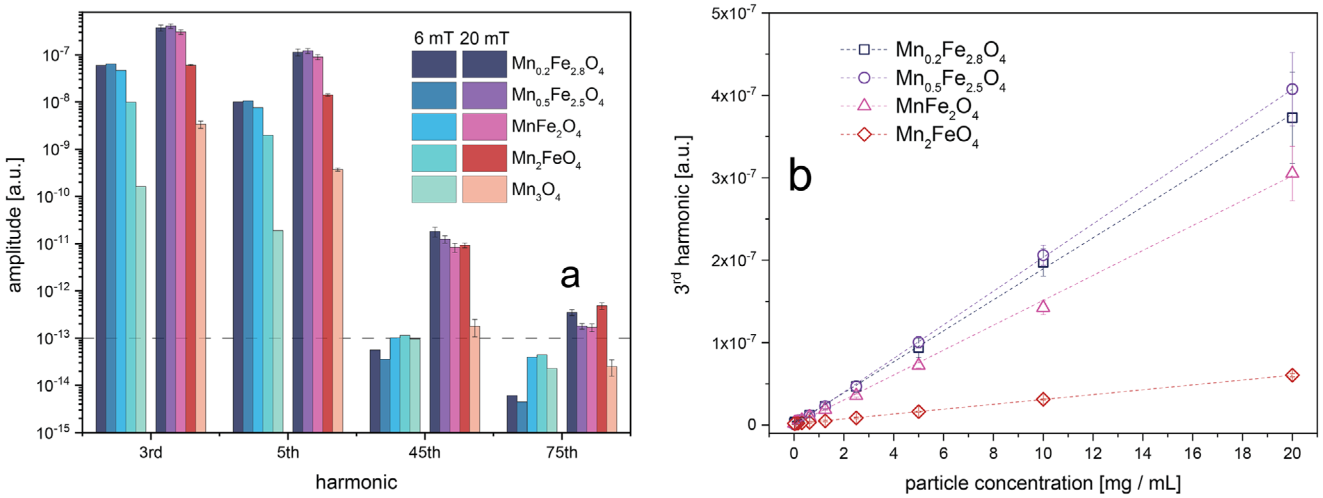

Figure 2. Magnetic particle spectroscopy results. a) Amplitude values for all Mn-ferrites at various harmonic frequencies were measured at 6 and 20 mT. b) Calibration lines. 3rd harmonic amplitude values as a function of particle concentration. (mean ± SD, N = 3).

$Mn_{0.2}Fe_{2.8}O_4$. This observation corresponds to the magnetic hysteresis data shown above (Figure 1e), where a curve shape dependence on the exact Mn content can be detected. Due to its weak and paramagnetic properties, Mn_3O_4 gives a strongly reduced signal. The signal dependence on the particle concentration was analyzed in Figure 2b, which depicts the calibration lines for the 3rd harmonic amplitudes. Mn_3O_4 was excluded due to its low signal. All shown particles show linear trends down to ≈100 µg mL^{-1} (see Figure S3, Supporting Information). The slopes of the calibration lines and thus the signal sensitivity to the particle amount decreases with increasing Mn content. $Mn_{0.5}Fe_{2.5}O_4$ attains the strongest 3rd harmonic amplitude of all investigated samples with 4.1×10^{-7} [a.u.] at 20 mg mL^{-1} and thus outperforms previously reported flame-made $Zn_{0.4}Fe_{2.6}O_4$ nanoparticles,[12] despite a smaller size.

2.2. Multicolor Imaging Using Different Ferrite Tracers

The accurate imaging of blocked blood flow, as well as of its successful restoration is of key importance for the in-time treatment of ischemia. A multi-color MPI approach is particularly interesting in this regard, as it allows the simultaneous imaging of different tracers injected, for example, at different time points, locations, or with varying surface properties. The here observed connections between the shape of the magnetization curves (Figure 1b), the MPS spectra (Figure 2a), and the Mn content incorporated into the iron oxide matrix suggest that our different tracers can not only be detected but also distinguished via MPI. To this end, system matrices for $Mn_{0.2}Fe_{2.8}O_4$ and Mn_2FeO_4 were obtained independently. Thereafter, they were imaged individually at different locations within a phantom, as well as in 50/50 mixed form. The reconstructed images can be seen in **Figure 3**a,b using the respective system matrices. Both the pure as well as the mixed samples could be clearly detected and localized, however only using the corresponding system matrix, as intended. The obtained signal intensities are quantitatively analyzed in Figure 3c, where the measured weight percentage is shown as a function of the nominal content. The images obtained via the $Mn_{0.2}Fe_{2.8}O_4$ system matrix result in excellent agreement with the predicted values, while the Mn_2FeO_4 counterpart shows a discrepancy of ≈28 wt.% for the pure $Mn_{0.2}Fe_{2.8}O_4$ sample. This highlights the tracers' applicability to multi-color MPI.

2.3. Enzyme-Like Properties of Mn-Ferrite Tracers

Following the successful localization of the ischemia, reperfusion of the hypoxic tissue due to the de-blocking of the blood supply will lead to increased ROS concentration. These in turn can lead to substantial damage to healthy cells. In this scenario, engineered catalytically active nanoparticles acting as so-called nanozymes can assist the heavily overstrained naturally occurring enzymes in the degradation of ROS to water and oxygen. In **Figure 4** we analyzed the enzymatic properties of our different Mn-ferrites both in acellular a) as well as in vitro b) assays. Two main steps in ROS degradation are typically described in the literature: I) highly reactive superoxide radicals (O_2^-) are converted into H_2O_2 via superoxide dismutase enzymes (or their mimics). II) H_2O_2 is degraded into H_2O and O_2 via catalase enzymes (or their mimics). Figure 4a analyzes the catalytic properties of the $Mn_xFe_{3-x}O_4$ nanoparticles in these reactions by depicting the respective converted ROS percentage (H_2O_2 left, O_2^- right). Increasing amounts of Mn in the iron oxide matrix leads to overall better enzymatic properties. Pure Mn_3O_4 shows the best performances, which can be explained by the highly interchangeable Mn^{2+}/Mn^{3+} oxidation states beneficial to the involved Fenton-like reaction. These seem superior to the Fe^{2+}/Fe^{3+} states of the iron oxide crystal. Furthermore, a better performance in the O_2^- compared to the H_2O_2 degradation can be observed for $Mn_{0.5}Fe_{2.5}O_4$ and $MnFe_2O_4$. This suggests a connection between the oxidative/reducing catalytic activity and the Mn/Fe ratio in the system. We further verified, that the prepared nanoparticles do not degrade H_2O_2 into harmful OH^- radicals (see Figure S4, Supporting Information), as previously partly reported for Mn-based systems.[31]

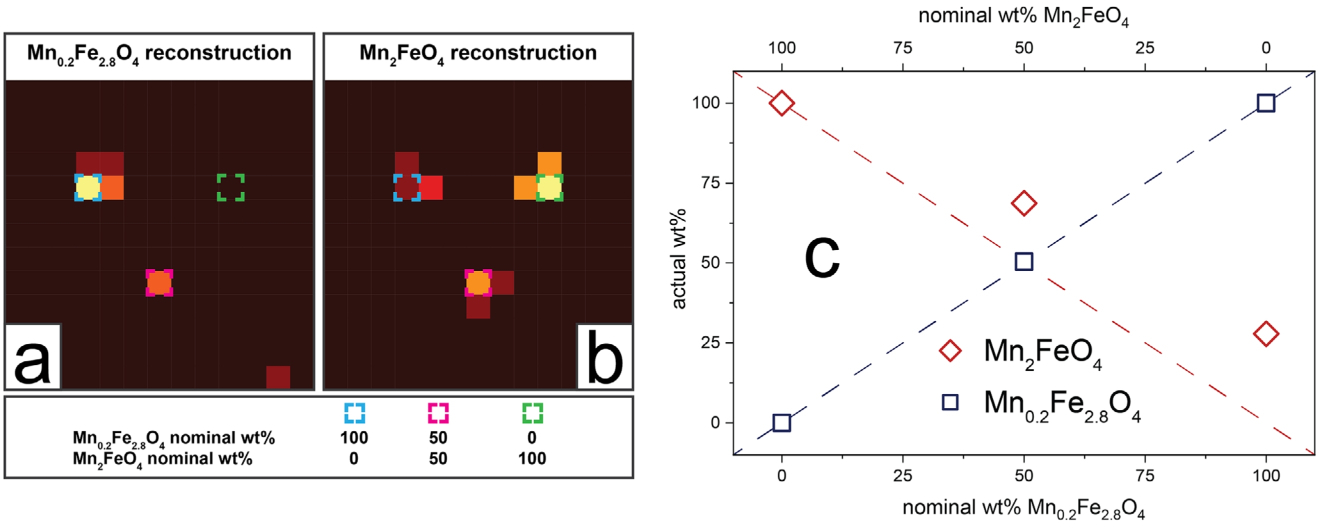

Figure 3. Multi-color magnetic particle imaging. Bare $Mn_{0.2}Fe_{2.8}O_4$ (blue squares), bare Mn_2FeO_4 (green squares) as well as half/half mixture (red squares) imaged via a) $Mn_{0.2}Fe_{2.8}O_4$ or b) Mn_2FeO_4 reconstruction. c) Quantitative analysis of images obtained in (a) and (b). Measured particle weight percentage as a function of nominal value for all three samples using $Mn_{0.2}Fe_{2.8}O_4$ (blue squares) or Mn_2FeO_4 (red diamonds) reconstruction.

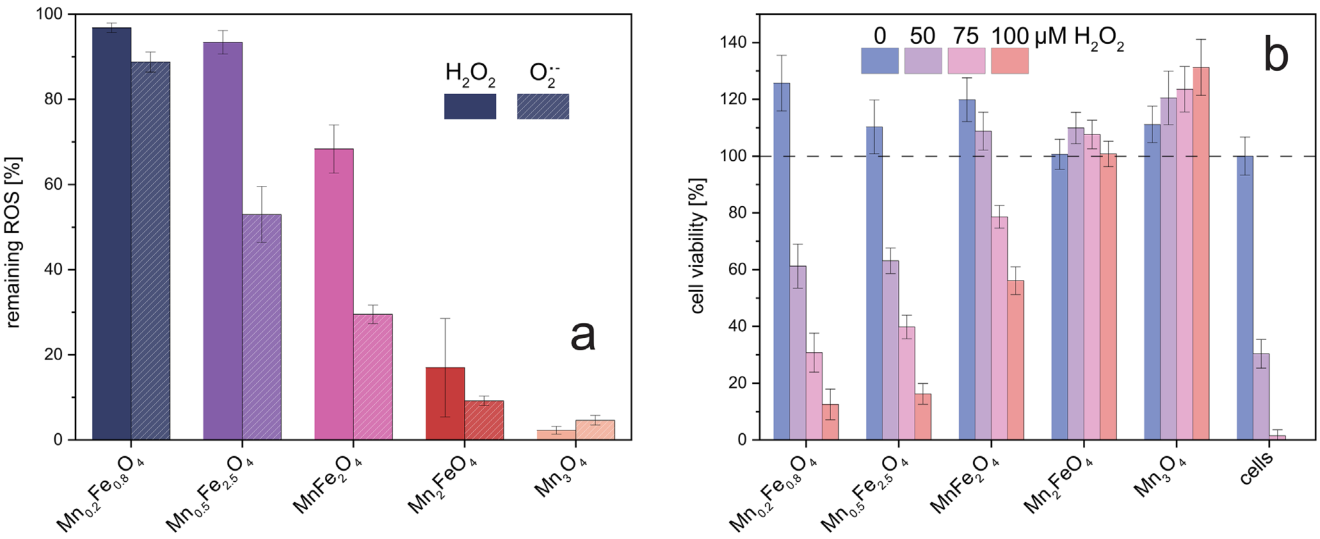

Figure 4. Reactive oxygen species scavenging capabilities of prepared Mn-ferrite particles. a) Remaining H_2O_2 (solid bars) and O_2^- (shaded bars) percentage after the addition of nanoparticle dispersion. b) 24 h cell viability after nanoparticle incubation (250 µg mL^{-1}, 2 h) and exposure to different H_2O_2 concentrations (22 h). (mean ± SD, N = 3).

These trends are further verified by the in vitro results shown in Figure 4b. The cells were incubated for 2 h with the various nanoparticles and exposed to different H_2O_2 concentrations thereafter. Their viability was determined after an additional 22 h. None of the samples alone (without H_2O_2) caused any substantial cytotoxicity at the investigated concentrations (see also Figure S5, Supporting Information). On the contrary, $Mn_{0.2}Fe_{2.8}O_4$ and $Mn_{0.5}Fe_{2.5}O_4$ showed even cytoprotective effects at elevated concentrations. As expected, increasing H_2O_2 concentrations resulted in pronounced cell death. This effect could be especially contradicted by the prepared nanozymes with high Mn content. While $Mn_{0.2}Fe_{2.8}O_4$ only slightly improved cell viability, Mn_2FeO_4 sufficiently degraded the added ROS even at 100 µM H_2O_2. Mn_3O_4 showed the best performance and, interestingly, lead to increased cell viability with increasing hydrogen peroxide concentrations. This can be explained by the high amounts of O_2 produced from the added H_2O_2 by the intra-cellular particles.

2.4. Hydrogen Peroxide Sensing via Mn-Ferrite Tracers

Triggered by the excellent enzyme-like properties of the prepared Mn-ferrites, we hypothesized substantial changes in the particles' surface oxidation states upon hydrogen peroxide exposure. This would further affect the magnetic properties and thus allow ROS sensing via magnetic particle spectroscopy. To this end, Mn_2FeO_4 particles (0.5 mg mL^{-1}) were exposed to 2.5 mM H_2O_2 and their

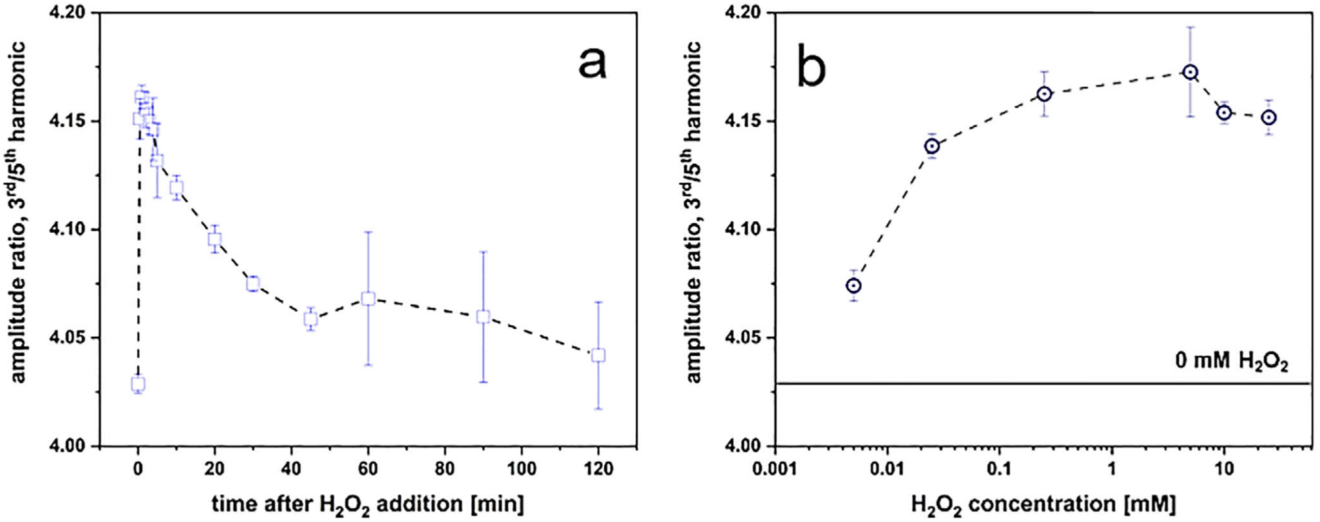

Figure 5. H_2O_2 sensing via magnetic particle spectroscopy (2nd/4th harmonic ratio) using Mn_2FeO_4 particles. a) Time-evolution of MPS signal after H_2O_2 addition. b) Calibration curve of MPS signal between 5 µm and 25 mm H_2O_2. (mean ± SD, N = 3).

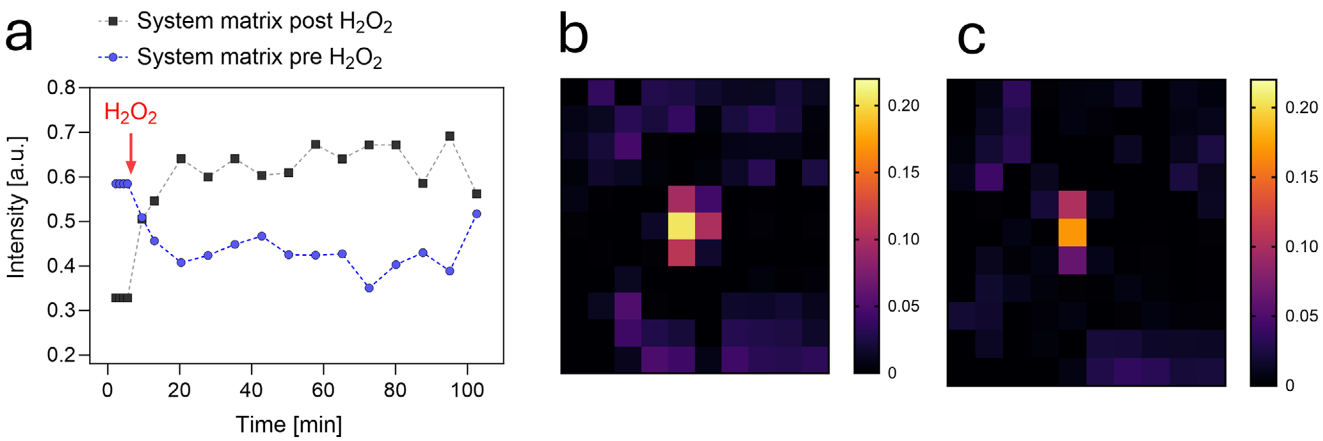

Figure 6. H_2O_2 sensing via magnetic particle imaging of Mn_2FeO_4 particles. a) Time-evolution of MPI signal after H_2O_2 addition (red arrow). Signal reconstructed via a system matrix recorded pre (blue circles) or post (black squares) H_2O_2 addition. 2-D magnetic particle images before b) and after 100 min c) of H_2O_2 addition.

MPS signal was recorded. **Figure** 5a shows the resulting 3rd to 5th amplitude ratio as a function of time. Compared to the initial pure water state, the ratio rapidly increases within seconds and stabilizes for ≈5 min before slowly recovering back to the H_2O_2-free state after roughly 1 h. A complete recovery is asymptotically reached after ≈2 h. This indicates a strong dependence of the MPS signal on ROS and thus structure oxidation state, with fast reaction times and complete recovery of the sensing elements.

Furthermore, the here used ratiometric signal approach (3rd to 5th amplitude ratio) allows an H_2O_2 sensing independent of the particle concentration, similar to previous temperature or viscosity detection methods via MPS.[32,33] To investigate the sensing performance in more detail, Figure 5b depicts the particle response to different H_2O_2 concentrations after 3 min. The system shows excellent sensitivity down to ≈25 µm. This falls clearly into the biomedically relevant H_2O_2 range.[34] At H_2O_2 concentrations above 250 µm the effect levels off, which most-likely can be explained by a surface saturation of the particle sensors. Overall, we attribute the change in the amplitude ratio, and consequently the general sensing mechanism, to an oxidation state-dependent magnetization. Due to the precise Mn doping achieved through the FSP synthesis process, magnetic and catalytically active Mn-ferrite particles are obtained. The catalytic decomposition of ROS triggers a concentration-dependent modulation in the oxidation state and MPS signal, while surface-regenerating effects lead to a time-dependent recovery to the initial state.(**Figure** 6)

Ultimately, the developed nanosensors shall be utilized for H_2O_2 sensing via magnetic particle imaging. To this end, the Mn_2FeO_4 particles at a concentration of 0.5 mg mL^{-1} were exposed to 2.5 mm H_2O_2 and the MPI signal recorded over time. The images were reconstructed using a system matrix recorded either before or after the H_2O_2 addition. The signal changes in line with the system matrix used, with both reconstruction methods demonstrating a clear and distinct response to H_2O_2 addition, consistent with the MPS data presented above. As anticipated, the shapes of the two curves are nearly inverted. The reconstructed images, showing a stronger signal before (b) than after H_2O_2 addition (c), confirm these observations, reinforcing that particle localization is effectively maintained even after H_2O_2 is introduced. Notably, data reconstructed using the pre- H_2O_2 system matrix tends to revert to its original H_2O_2-free state, while data reconstructed with the post- H_2O_2 system matrix remains elevated even after 100 minutes, suggesting unique interactions that will be an exciting area for future research.

3. Conclusion

Although the restoration of blood flow is the key treatment step of ischemia, it can paradoxically also lead to severe tissue damage following the resulting elevated oxygen and ROS levels. Here, novel multifunctional Mn-ferrite MPI nanotracers for the detection, imaging, and treatment of this ischemia-reperfusion injury have been developed. The utilized highly scalable flame synthesis enabled the fine-tuning of the particles' magnetic properties by varying the Mn content in the iron oxide matrix. The two extreme systems ($Mn_{0.2}Fe_{2.8}O_4$ and Mn_2FeO_4), which both showed excellent MPI properties, were investigated in a multi-color MPI approach. Next to their promising performance as MPI tracers, we showed the outstanding enzyme-like properties of the prepared Mn-ferrite nanoparticles. Both dye-based assays, as well as the in vitro tests, highlighted the system's capability of efficiently degrading reactive oxygen species, such as OH^- and H_2O_2. As such they outperformed previously reported CeO_2 or Fe_2O_3 nanoparticles. We explain this by the highly interchangeable oxidation states of both Mn and Fe atoms in the crystal structure. Next, we hypothesized that these changing oxidation states should also affect the magnetic properties of the particles. This claim was confirmed by exposing the Mn_2FeO_4 structures to H_2O_2 and measuring the MPS as well as MPI signal over time. We detected a clear dependency of the signals on both H_2O_2 concentration and time-after exposure. To the best of our knowledge, this for the first time demonstrates ROS sensing via magnetic particle spectroscopy and/or imaging. Opposed to previous MPS sensing approaches for temperature or viscosity, the here reported technology relies on direct changes to the surface of the nanomaterial. This potentially makes this system more robust against other influences, which will be the topic of further research, also in vivo. In the future, various surface modification strategies could be applied to Mn-ferrite particles to ensure long-term stability or targeted delivery. Such modifications should be carefully selected to avoid impairing—and ideally, further enhance—the catalytic activity.[35] In summary, our Mn-ferrite nanosystems are proposed as a promising diagnostic and therapeutic platform for the cardiovascular field, enabling the imaging, sensing, and degradation of ROS.

4. Experimental Section

Particle Synthesis: Nanoparticles were produced by flame spray pyrolysis, as previously described.[13,14] In brief manganese(II) nitrate tetrahydrate (purum p.a. ≥97.0% (KT), Sigma–Aldrich) and iron(III) nitrate nonahydrate (ACS reagent, ≥98%, Sigma–Aldrich) were dissolved under magnetic stirring in a 1:1 (by volume) mixture of ethanol absolute (VWR Chemicals) and 2-ethylhexanoic acid (99%, Sigma–Aldrich). The total metal (Mn + Fe) concentration in the precursor was kept constant at 0.3 M and the Mn/Fe ratio adapted to the nominal values in the respective particle samples. The liquid precursor was then fed at 8 mL min^{-1} through a capillary and dispersed into fine droplets by 5 L min^{-1} O_2. The droplets are then ignited by a premixed CH_4/O_2 (1.5/3.2 L min^{-1}) flamelet, which results in the particle formation downstream. The produced materials were then collected on a glass-fiber filter (Whatman GF6, 257 mm diameter) with the aid of a vacuum pump (Busch, Seco SV 1040C). The particles were used as synthesized and were well-dispersible in water because of their relatively hydrophilic surface.

Characterization: X-ray diffraction patterns were recorded on a Bruker D2 Phaser. The data was analyzed with Diffrac Eva and Topas 4 software. Crystal structures were identified via ICSD 08 4611 ($Mn_xFe_{3-x}O_4$) and 68 174 (Mn_3O_4). Crystal sizes were obtained via the Scherrer equation. Scanning transmission electron microscopy (STEM) was performed on a Talos F200x microscope (ThermoFisher, field emission gun at 200 kV) with four attached silicon drift detectors. Samples were prepared by dispersing nanoparticles in mili-Q ultra-pure water. A dispersion drop was deposited on a carbon-coated copper grid (EMR, Lacey Carbon Film 200 Mesh Copper) and then carefully dried. About 60 individual particles each were measured to evaluate the size distribution as geometric mean. Dynamic light scattering and surface charge (Zeta potential) measurements were conducted using a Zetasizer (Nano ZS90, Malvern Instruments). The nanoparticles were dispersed at a concentration of 0.1 mg mL^{-1} in H2O and sonicated for 10 min (Ultrasonic Processor, pulses: 28 s/2s, 90% Amplitude) prior the measurement.

Catalytic Activity Assays: To assess H_2O_2 scavenging activity of nanoparticles, a 25 µg mL^{-1} nanoparticle dispersion was incubated in 50 mM H_2O_2 (88 597, Sigma Aldrich) for 1 h at 37 °C. To ensure a homogenously dispersed solution, the particle solution was sonicated beforehand, and vortexed every 15 min during incubation time. Afterward, the sample was centrifuged at maximal speed for 15 min. Part of the remaining supernatant was collected and diluted 1:1 in Milli-Q water. The remaining H_2O_2 concentration in the diluted samples was assessed by measuring the absorbance at 240 nm. A standard curve was also measured to estimate the absolute H_2O_2 concentration. To determine whether the H_2O_2 decomposition was attributed to CAT- or POD-like activity of nanoparticles, an additional assay was performed to detect OH^- generation by an aminophenyl fluorescein (APF) fluorescence indicator. 5 µM APF (A4108, Sigma–Aldrich) were mixed with a 100 µg mL^{-1} particle solution in Tris HCl buffer (0.1 M) and 1 mM H_2O_2, vortexed, and incubated at 37 °C for 30 min. Thereafter the fluorescent intensity was measured at 535 nm with excitation at 485 nm using a plate reader (Infinite F200 Pro, TECAN). The superoxide (O_2^-) scavenging activity was quantified by a colorimetric method using WST-1 (2-(4-Iodophenyl)- 3-(4-nitrophenyl)-5-(2,4-disulfophenyl)- 2Htetrazolium, monosodium salt). For that 1.25 µg mL^{-1} nanoparticle solution in Tris HCl buffer (0.1 M), 0.056 mM WST-1 solution in Assay buffer (1 µM Hypoxanthine (H9377, Sigma Aldrich) in 0.1 M Tris HCl buffer) and 9 mU mL^{-1} Xanthine oxidase (X4875, Sigma–Aldrich) were mixed, sonicated, and incubated at 37 °C for 5 min. During incubation time, samples were protected from light. Subsequently, the reaction solution was centrifuged at maximal speed for 15 min. The remaining supernatant was retrieved and used to determine the SOD activity by absorbance reading at 440 nm.

Cell Viability and Protection: Human gingival fibroblasts (hGF) were cultured, passaged, and kept going in a cell culture flask in an incubator at 37 °C and 5% CO_2. To perform cell-based assays, hGFs were seeded in a well plate with a density of 20′000 cells cm^{-2} 24 h prior to intervention. To determine the toxicity of nanoparticles on cells, nanoparticle solutions ranging from 50 to 1000 µg mL^{-1} were dispersed in high-glucose Dulbecco's Modified Eagle's (D5796, Sigma–Aldrich) supplemented with 10% fetal bovine serum (F9665, Sigma–Aldrich), 1% L-glutamine (59292C, Sigma–Aldrich), and 1% penicillin−streptomycin−neomycin solution (P4083, Sigma–Aldrich). The particle-medium mix was left to rest for 30 min to enable formation of a protein corona around the nanoparticles before its addition to the cells. After 24 h incubation at 37 °C and

5% CO_2, the cells were washed with prewarmed DPBS (D8537, Sigma–Aldrich) three times, before assessing the cell viability by the CellTiter 96 AQueous One Solution Cell Proliferation Assay (Promega, G3580). The cells reacted with the AQueous One solution reagent (317 µg mL^{-1} MTS) for 1 h at 37 °C, 5% CO_2 prior to the absorbance readout at 490 nm.

To estimate the extent to which the nanoparticles protect cells from ROS, a modified viability assay was performed. 0, 50, 75, or 100 mM H_2O_2 was added to the cells, which were previously incubated with 250 µg mL^{-1} nanoparticles for 2 h. All was incubated for the remaining 22 h before cell viability was assessed as described above.

Magnetic Particle Spectroscopy: Magnetic particle spectroscopy (MPS) was measured with a commercial MPS device (MPS-3, Bruker BioSpin GmbH & Co. KG, Germany). The MPS operates at a fixed excitation frequency of $f_0 = 25.25$ kHz and variable excitation field amplitudes B_{ex} between 0.05 and 25 mT. An excitation field of $B_{ex} = 6$ mT or $B_{ex} = 20$ mT was used for all measurements. Samples were filled into PCR tubes, using 20 µL sample for each measurement, with data averaging of 10 s. Consequently, for hydrogen peroxide sensing 10 µL of Mn_2FeO_4 particles (0.5 mg mL^{-1}) were mixed with 10 µL 2.5 mM H_2O_2 and MPS spectra were recorded from 0.5 to 120 min. Different concentrations of Mn_2FeO_4 ranging from 1 to 0.0625 mg mL^{-1} were measured for particle calibration lines, while different concentration of H_2O_2 ranging from 5 µM to 25 mM were chosen for the particle response. The resulting MPS spectra were recorded 3 min after adding H_2O_2 to the sample each.

Magnetic Particle Imaging: Magnetic particle imaging (MPI) measurements were performed using the MPI 25/20FF preclinical system (Bruker BioSpin GmbH & Co. KG, Ettlingen, Germany). A 2D sinusoidal excitation of 12 mT amplitude and a selection field with a gradient strength of 0.85 T m^{-1} were set. Two system matrices were measured on an 11 × 11 equidistant grid using a 3 mm × 3 mm × 20 mm delta sample containing 180 µL of Mn_2FeO_4 particles (0.5 mg mL^{-1}). System matrices were taken before and 2 h after the addition of 100 µL of H_2O_2 (2.5 mM). A total of 18 2D measurements were taken with the same delta sample placed at the center of the field of view during these 2 h after H_2O_2 addition. Each measurement was averaged over 30 frames. Reconstruction was performed using the Kaczmarz method with 2000 iterations and L_2 regularization via the open-access Julia package MPIReco.

Statistical Analysis: Catalytic activity assays, cell viability and protection assays and magnetic particle spectroscopy measurements were conduced as 3 independent experiments, representing the results as (mean ± SD, N = 3). Magnetic Particle Imaging data was processed by the open-access Julia package MPIReco. Software used for statistical analysis included OriginPro 2025 and GraphPad Prism 10.

Supporting Information

Supporting Information is available from the Wiley Online Library or from the author.

Acknowledgements

The authors acknowledge funding from the Swiss National Science Foundation (Excellenza grant no. 181290, I.K.H), the Scientific Exchange scheme (IZSEZ0_205894) and the ETH Zurich Foundation (ETH Career Seed Grant).

Conflict of Interest

The authors declare no conflict of interest.

Data Availability Statement

The data that support the findings of this study are available in the supplementary material of this article.

Keywords

magnetic particle spectroscopy, nanozyme, sensor, theranostics, tissue injury

Received: December 4, 2024
Revised: April 7, 2025

---

[1] H. K. Eltzschig, T. Eckle, *Nat. Med.* **2011**, *17*, 1391.
[2] M.-Y. Wu, G.-T. Yiang, W.-T. Liao, A. P.-Y. Tsai, Y.-L. Cheng, P.-W. Cheng, C.-Y. Li, C.-J. Li, *Cell. Physiol. Biochem.* **2018**, *46*, 1650.
[3] T. Knopp, T. M. Buzug, *Magnetic Particle Imaging*, Springer Heidelberg, Berlin **2012**.
[4] B. Gleich, J. Weizenecker, *Nature* **2005**, *435*, 1214.
[5] J. Franke, N. Baxan, H. Lehr, U. Heinen, S. Reinartz, J. Schnorr, *IEEE Transat. Med. Imaging* **2020**, *39*, 4335.
[6] P. Ludewig, N. Gdaniec, J. Sedlacik, N. D. Forkert, P. Szwargulski, M. Graeser, G. Adam, M. G. Kaul, K. M. Krishnan, R. M. Ferguson, A. P. Khandhar, P. Walczak, J. Fiehler, G. Thomalla, C. Gerloff, T. Knopp, T. Magnus, *ACS Nano* **2017**, *11*, 10480.
[7] P. Szwargulski, M. Wilmes, E. Javidi, F. Thieben, M. Graeser, M. Koch, C. Gruettner, G. Adam, C. Gerloff, T. Magnus, T. Knopp, P. Ludewig, *ACS Nano* **2020**, *14*, 13913.
[8] J. Weizenecker, B. Gleich, J. Rahmer, H. Dahnke, J. Borgert, *Phys. Med. Biol.* **2009**, *54*, L1.
[9] J. Rahmer, A. Halkola, B. Gleich, I. Schmale, J. Borgert, *Phys. Med. Biol.* **2015**, *60*, 1775.
[10] N. Silvestri, H. Gavilán, P. Guardia, R. Brescia, S. Fernandes, A. C. S. Samia, F. J. Teran, T. Pellegrino, *Nanoscale* **2021**, *13*, 13665.
[11] Y. Du, X. Liu, Q. Liang, X.-J. Liang, J. Tian, *Nano Lett.* **2019**, *19*, 3618.
[12] L. Moor, S. Scheibler, L. Gerken, K. Scheffler, F. Thieben, T. Knopp, I. K. Herrmann, F. H. L. Starsich, *Nanoscale* **2022**, *14*, 7163.
[13] F. H. L. Starsich, C. Eberhardt, A. Boss, A. M. Hirt, S. E. Pratsinis, *Adv. Healthcare Mater.* **2018**, *7*, 1800287.
[14] F. H. L. Starsich, G. A. Sotiriou, M. C. Wurnig, C. Eberhardt, A. M. Hirt, A. Boss, S. E. Pratsinis, *Adv. Healthcare Mater.* **2016**, *5*, 2698.
[15] F. H. L. Starsich, I. K. Herrmann, S. E. Pratsinis, *Annu. Rev. Chem. Biomol. Eng.* **2019**, *10*, 155.
[16] J. Wu, X. Wang, Q. Wang, Z. Lou, S. Li, Y. Zhu, L. Qin, H. Wei, *Chem. Soc. Rev.* **2019**, *48*, 1004.
[17] S. Singh, *Biointerphases* **2016**, *11*, 04B202.
[18] M. T. Matter, L. A. Furer, F. H. L. Starsich, G. Fortunato, S. E. Pratsinis, I. K. Herrmann, *ACS Appl. Mater. Interfaces* **2019**, *11*, 2830.
[19] S. Cai, R. Yang, in *Nanozymology: Connecting Biology and Nanotechnology*, (Ed. X. Yan), Springer, Berlin, Germany **2020**, pp. 331–365.
[20] S. Yu, H. Zhang, S. Zhang, M. Zhong, H. Fan, *Front. Chem.* **2021**, *9*, 651053.
[21] J. Yao, Y. Cheng, M. Zhou, S. Zhao, S. Lin, X. Wang, J. Wu, S. Li, H. Wei, *Chem. Sci.* **2018**, *9*, 2927.
[22] G. Yuan, H. Ding, H. Sun, L. Zhou, Q. Lin, *Sens. Actuators, B* **2019**, *296*, 126706.
[23] A. Pratsinis, G. A. Kelesidis, S. Zuercher, F. Krumeich, S. Bolisetty, R. Mezzenga, J.-C. Leroux, G. A. Sotiriou, *ACS Nano* **2017**, *11*, 12210.
[24] H. Wu, R. Nißler, V. Morris, N. Herrmann, P. Hu, S.-J. Jeon, S. Kruss, J. P. Giraldo, *Nano Lett.* **2020**, *20*, 2432.
[25] S. Duanghathaipornsuk, E. J. Farrell, A. C. Alba-Rubio, P. Zelenay, D.-S. Kim, *Biosensors* **2021**, *11*, 30.
[26] G. Liu, J. Hall, N. Nasiri, T. Gengenbach, L. Spiccia, M. H. Cheah, A. Tricoli, *ChemSusChem* **2015**, *8*, 4162.
[27] R. Strobel, S. E. Pratsinis, *Adv. Powder Technol.* **2009**, *20*, 190.

[28] A. M. Hirt, G. A. Sotiriou, P. R. Kidambi, A. Teleki, *J. Appl. Phys.* **2014**, *115*, 044314.

[29] H. Yang, C. Zhang, X. Shi, H. Hu, X. Du, Y. Fang, Y. Ma, H. Wu, S. Yang, *Biomaterials* **2010**, *31*, 3667.

[30] J. Xie, S. Peng, N. Brower, N. Pourmand, S. X. Wang, S. Sun, *Pure Appl. Chem.* **2006**, *78*, 1003.

[31] J. Kim, H. Y. Kim, S. Y. Song, S. Go, H. S. Sohn, S. Baik, M. Soh, K. Kim, D. Kim, H.-C. Kim, N. Lee, B.-S. Kim, T. Hyeon, *ACS Nano* **2019**, *13*, 3206.

[32] J. Zhong, M. Schilling, F. Ludwig, *Phys. Rev. Appl.* **2021**, *16*, 054005.

[33] C. Stehning, B. Gleich, J. Rahmer, *Int. J. Magnet. Part. Imag.* **2016**, *2*, eaal2845.

[34] V. Rani, S. Mishra, T. Yadav, U. C. S. Yadav, S. Kohli, in *Free Radicals in Human Health and Disease*, (Eds. V. Rani, U. C. S. Yadav), Springer, Berlin, Germany **2015**, pp. 105–116.

[35] R. Nißler, L. Dennebouy, A. Gogos, L. R. H. Gerken, M. Dommke, M. Zimmermann, M. A. Pais, A. L. Neuer, M. T. Matter, V. M. Kissling, S. de Brot, I. Lese, I. K. Herrmann, *Small* **2024**, *20*, 2311115.